ORIGINAL PAPER

Finite element analysis on mechanical state on the osteoclasts under gradient fluid shear stress

Xiao Zhang[1] · Qing Sun[1] · Chongyang Ye[1] · Taiyang Li[1] · Fei Jiao[1] · Yan Gao[1] · Bo Huo[1]

Abstract

Mechanical loading, such as fluid shear stress (FSS), is regarded as the main factor that regulates the biological responses of bone cells. Our previous studies have demonstrated that the RAW264.7 osteoclast precursors migrate toward the low-FSS region under the gradient FSS field by a cone-and-plate flow chamber, in which the FSS in the outer region is larger than that in the inner region along the radial direction. Whether the FSS distribution on a cell depends on the gradient direction of FSS field should be clarified to explain this experimental observation. In this study, the finite element models of the discretely distributed or closely packed cells adherent on the bottom plate in a cone-and-plate flow chamber were constructed, and cells were regarded as compressible isotropic Hookean solid. Results showed that the average FSS of each discretely distributed cell at the quarter sector far from the center (SFC) was about 0.1% greater than that at the quarter sector near the center (SNC). In the bands with different orientations for a cell, the relative difference between the average FSS in the SFC and the SNC becomes smaller with increased band height. For the hexagonal closely packed cells, the relative value of SFC and SNC increases with increasing cell spacing. The difference between the local wall FSS in the SFC and the SNC may activate mechanosensitive ion channels and further regulate the migration of osteoclast precursors toward the low-FSS region under the gradient FSS field.

Keywords Cone-and-plate chamber · Fluid shear stress · Mechanical state · Finite element analysis · Cell migration

1 Introduction

Bone remodeling is an important physiological process characterized by bone formation and absorption. Once subjected to mechanical loading, the structure of the bone tissue is optimized through the bone remodeling process (George et al. 2020, 2018; Giorgio et al. 2020; Robling et al. 2006). One key issue in clarifying the mechanism of the mechanical loading-induced bone remodeling is to explain the migration of osteoclast precursors for the targeting of the sites of bone resorption especially around the microdamages within the bone matrix. Our previous studies have demonstrated the

field of the gradient fluid shear stress (FSS) around bone microdamages (Gao et al. 2019b). Two types of flow chamber (i.e., cone-and-plate and parallel-plate flow chambers), which can apply the gradient FSS on the cells adherent on the bottom plate, are constructed (Gao et al. 2019a, b; Ye et al. 2019). Experimental results show that the osteoclast precursor RAW264.7 cells can sense this gradient FSS and migrate toward the region with low FSS (Gao et al. 2019b). However, the underlying mechanism of this experimental observation has not been clarified.

The parallel-plate flow chamber is commonly used to apply the FSS on cells in vitro (McAllister et al. 2000), but the prominent disadvantage of this device is its tedious operation procedure and high frequency of cell contamination. The cone-and-plate flow chamber is constructed in our laboratory on the basis of a standard 6-well culture plate to exert fluid flow on cells for long-term culture (Ye et al. 2019). By modifying the cone's generatrix, this device can provide FSS as high as 1 or 2 Pa with uniform distribution or constant gradient over the majority of the plate. The finite element analysis (FEA) shows that for the cone-and-plate

✉ Yan Gao
7520190087@bit.edu.cn

✉ Bo Huo
huobo@bit.edu.cn

[1] Biomechanics Lab, Department of Mechanics, School of Aerospace Engineering, Beijing Institute of Technology, No. 5 South Zhongguancun Street, Beijing 100081, People's Republic of China

flow chamber with the gradient FSS field, the FSS in the center of the bottom plate is lower than that in the outer region (Gao et al. 2019b). However, whether the distribution of the wall FSS on the surface of one cell depends on the gradient of FSS remains unknown. Some studies have found that the cell migration may be influenced by the intracellular calcium distribution but is important to explore whether the calcium ion channels in different locations of the cell membrane are activated at different levels through the distribution of the FSS on the cell.

In the present study, finite element (FE) models for the discretely distributed or closely packed cells on the bottom plate are constructed. The FEA is performed on the models to investigate the effect of the cell distance on the FSS distribution on a cell and clarify whether the FSS at different locations of the cell depends on the gradient of the FSS field.

2 Methods

2.1 Cone-and-plate flow chamber

A custom-made cone-and-plate chamber was adopted to produce a flow field with the gradient wall FSS. This device consisted of motor, cone, and regular 6-well culture plate. Each motor was connected to a cone, and the cone's rotation applied shear fluid flow on the cells cultured on the plates. The photograph and schematic of the 1-well plate device are shown in Fig. 1A and B. The FE meshing for this device with five cells placed on the plate along the radical direction

and that for one of the cells is shown in Fig. 1C and D. The motorized rotation of the cone drives the medium in culture plate to flow over cells cultured on the plate. The wall FSS exerted on the cell was controlled by specifying the cone's rotation speed.

2.2 Material property of cells

In this study, the hyperelastic model with compressible isotropic Hookean material property was adopted for the cells with 10 μm in the radius. A simple non-negative strain energy density W_s for a compressible isotropic Hookean material is proposed here (Attard 2003; Simo and Pister 1984):

$$W_s = \frac{1}{2}G(I_\lambda - 3) + \frac{1}{2}\Lambda(\ln J)^2 - G\ln J, \qquad (1)$$

in which I_λ and J are the invariants of stretch tensors. The material constants G and Λ are defined by:

$$G = \frac{E}{2(1+\mu)} \text{ and } \Lambda = \frac{E\mu}{(1+\mu)(1-2\mu)} \qquad (2)$$

In the above expression, E, G, μ, and Λ denote the elastic modulus, shear modulus, Poisson's ratio, and the Lamé constant, respectively. The Poisson's ratio must be less than 0.5 and greater than -1 to guarantee that the strain energy density is positive for all deformations (Attard 2003). Table 1 presents the specific material properties for the cells used in this study.

Fig. 1 Cone-and-plate flow chamber and FE model. **A** Custom-made cone-and-plate flow chamber. **B** Schematic of the cone-and-plate flow chamber, where h_0 is the distance of the cone's tip above the bottom of the plate, h_c is the height of the cone, θ is the angle between the cone's generatrix and the plate, ω is the angular velocity of the cone (18 rad/s), and R is the radius of the well. **C** Mesh of the FE model for the cone-and-plate flow chamber. **D** Enlarged view of one cell's mesh
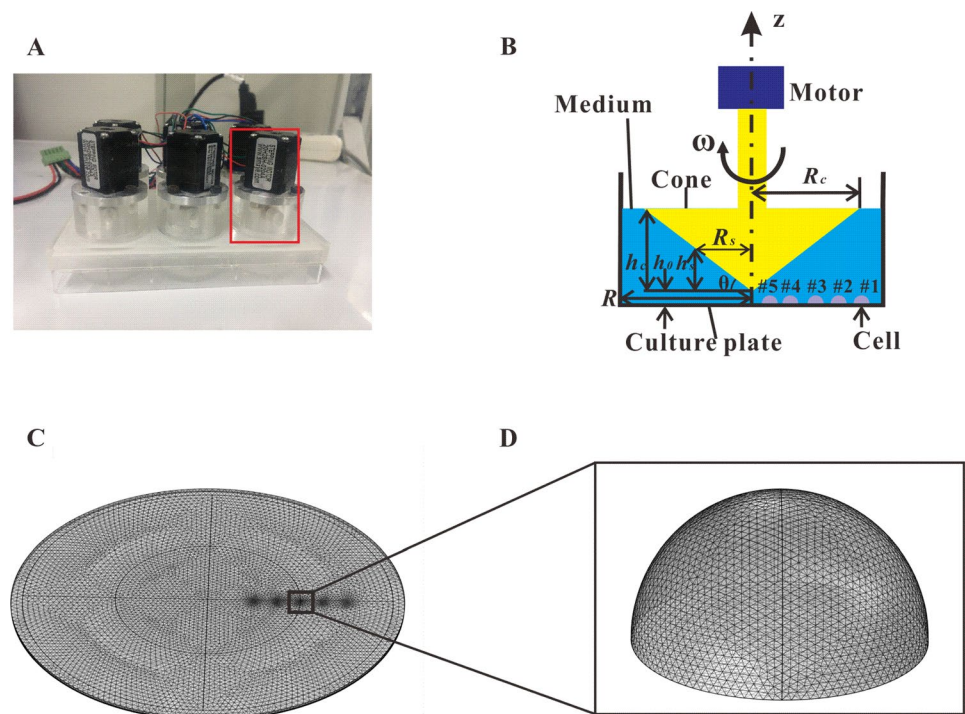
Material property	Values for osteoclast precursors
Cell density (ρ, kg/m^3)	1100 (Grover et al. 2011)
Poisson's ratio (μ)	0.3 (McGarry and Prendergast 2004)
Young's modulus (E, N/m^2)	5000 (Xue et al. 2015)
Lamé constant (Λ, N/m^2)	2885
Shear modulus (G, N/m^2)	1923

2.3 Data analysis considering the secondary flow

The secondary flow of fluid flow should be considered in a cone–plate apparatus when the nondimensional Reynold number (Re) is between 0.5 and 4.0 (Sdougos et al. 2006). The cone-and-plate flow chamber used in this study modified the cone's shape. The cone's generatrix was not as linear as the traditional cone–plate apparatus. The FEA results showed that this may cause secondary flow revealed by the streamline around a cell (Fig. 2A). The angle between the fitted line and the *x* axis was about 10°. The FSS contour on the cell surface was ellipse-like with an angle of about 10° to the *x* axis (Fig. 2B, C), which was caused by secondary flow. The surface of each cell was divided into two parts, whose projections at the bottom plate were quarter sectors with central lines perpendicular to the actual flow direction, i.e., the sector far from the center (SFC) and the sector near the center (SNC), to consider the effect of the secondary flow on the FSS distribution. In addition, two types of data analysis methods, i.e., average FSS values of whole SFC and SNC regions and bands with orientations of 30°, 45°, and 60° relative to the sphere center, were established (Fig. 2D–G).

2.4 Numerical simulation

The flow field was numerically simulated using the FEA through the COMSOL Multiphysics software. Navier–Stokes equations were used to describe the flow behavior of the momentum conservation in the cone-and-plate chamber, and the fluid was assumed to be viscous and incompressible with density (ρ) of 1×10^3 kg/m^3 and viscosity of 1×10^{-3} Pa·s. The cone's generatrix was polyline to establish a wall FSS field with constant gradient on the plate surface. The radius of the polyline point (R_s) was 8 mm, and its vertical distance (h_s) to the cone's tip was 0.05 mm. The total radius (R_c) of the cone was 16 mm, and its vertical distance (h_c) to the tip was 0.15 mm. The gap (h_0) between the cone's tip and the plate surface was 0.4 mm. The angular velocity of the cone was 172 rpm. The radius (R) of a well for the 6-well culture plate was 17 mm. The no-slip boundary condition was assumed for all rigid surfaces in the model except for the cone, and a free-surface boundary condition was used for the upper fluid surface within the well. The circular surface

at the bottom of each cell was identified as a fixed constraint. Data analysis was performed using the MATLAB software.

3 Results

3.1 Average FSS in the SFC is significantly higher than that in the SNC for discretely distributed cells

When cells were discretely distributed on the plate along the radial direction, FE models were constructed to calculate the FSS field on the plate and the cell surface (Fig. 3A). The mesh sensitivity test revealed that when the number of total elements was bigger than about 1.02 million, the calculation of FSS on the cell surface converged (Fig. 3B). Therefore, this element number was adopted in all models in this study. The wall FSS distribution on the plate displayed a linear relationship with the distance to the center and ranged from 0.1 to 0.65 Pa (Fig. 3C, D). This finding also indicated the existence of a gradient wall FSS field on the plate for a cone-and-plate flow chamber. When different numbers of cells were radially arranged, the FSS on the top region of the cell surface was higher than that close to the adhesion region (Fig. 3E, F). For models with 1, 3, or 5 cells, the average FSS in the SFC was higher than that in the SNC in most cells (Fig. 3G–I). The relative difference was statistically summarized, and almost all values were positive except the #3 cell in the second group, indicating that the average FSS in SFC was larger than that in the SNC (Fig. 3J). If the secondary flow was not considered, all relative values were positive (Supplementary Fig. 1A–D). The above results showed that the gradient FSS field in the whole plate of a cone-and-plate flow chamber led to the gradient distribution of average FSS within a cell along the radial direction, i.e., high in SFC and low in SNC (abbreviated to HFLN).

3.2 FSS in the region of a cell close to the adhesion substrate reveals high level of HFLN for discretely distributed cells

The average values of FSS on the bands with different orientations of 30°, 45°, or 60° in the SFC and the SNC were compared to investigate whether different regions along the height direction of a cell also had the HFLN phenomenon (Fig. 4A–I). The relative values of the average FSS between the bands in the SFC and the SNC with the same orientation in each cell were obtained (Fig. 4J). Almost all relative values were positive, and only the relative value at 60° was negative, suggesting that the average FSS in the bands in the SFC were larger than that in the SNC. In addition, the relative value became smaller with increasing band orientation. When the section choice did not involve the secondary flow, the average

Fig. 2 Effect of the secondary flow on the FEA. **A** Streamline flowing around a cell. The green line is obtained by linearly fitting the black dots. **B** The contour map of FSS on the cell surface is ellipse-like with a certain angle to the *x* axis. **C** A contour ellipse labeled with a red dash line is fitted with the FSS contour with 0.32 Pa. The angle between the short axis of the fitted ellipse and the *y* axis is about 10°. Two types of data analysis methods are introduced in **D** and **E**. **D** Surface of one cell divided into two sectors with ± 45° relative to the *x* axis. Gray parts of the SFC and the SNC are used to calculate the average FSS. When considering the direction of the secondary flow, the above sectors are rotated anticlockwise by 10° and labeled by red dotted lines, which are used in most cases in this study. **E** Bands on the cell surface with three orientations, i.e., 30°, 45°, and 60°, shown in red lines in the SFC and in green lines in the SNC. Top views of the bands with different orientations in the sectors considering **F** with and **G** without the secondary flow
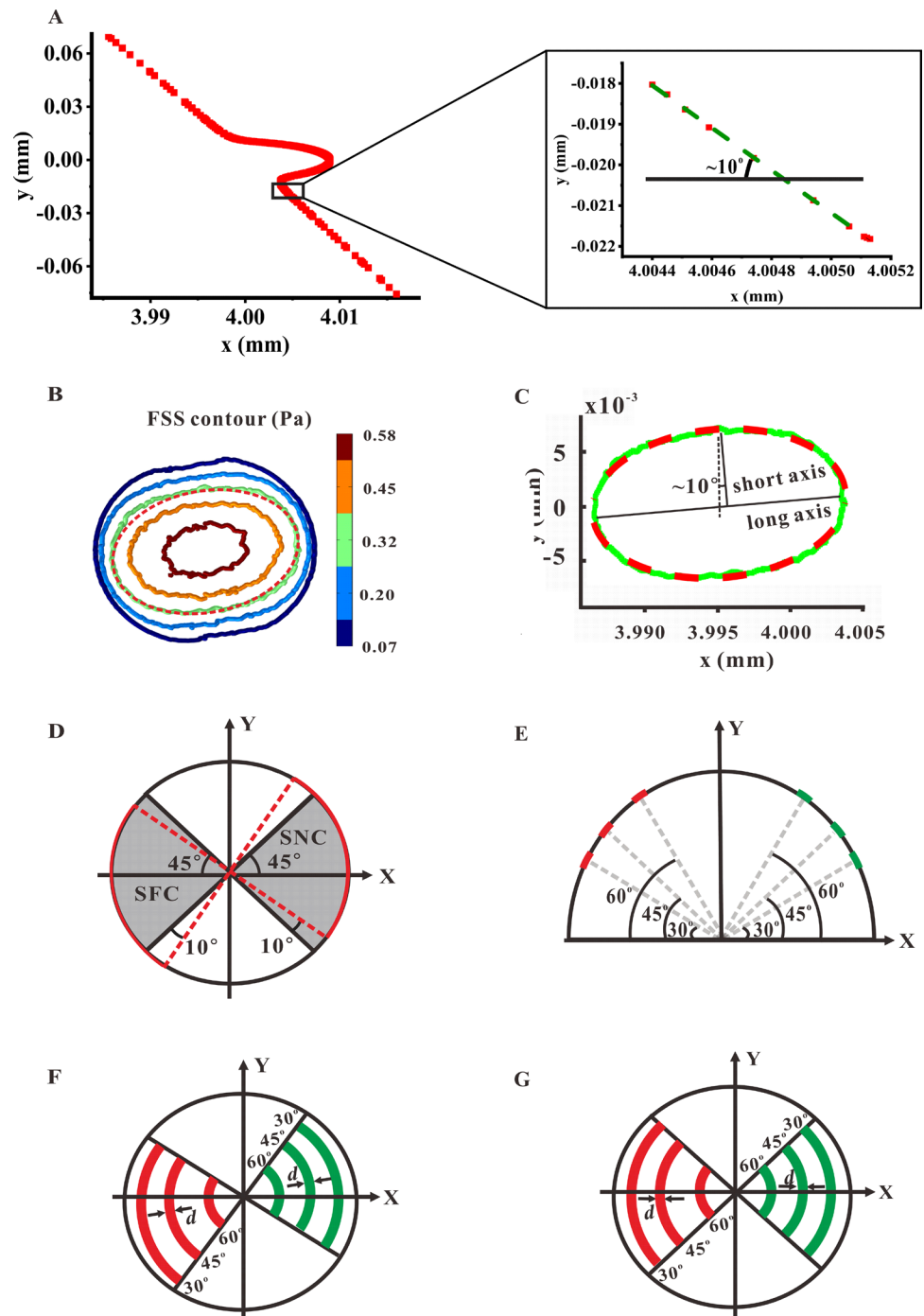
FSS of some bands in the SFC were smaller than that in the SNC, and the relative value became small or even negative in the region close to the top of a cell (Supplementary Fig. 2A–J).

3.3 HFLN phenomenon is reduced for hexagonal closely packed cells approaching each other

The hexagonal closely packed arrangement with two cell spacing was constructed in different locations along the radial direction to study the effect of neighboring cells on the FSS field on the surface of a cell (Fig. 5A). Only central cells were analyzed, and their meshes were refined to maintain the computation accuracy (Fig. 5B). Results showed that the FSS distribution on the cell surface also revealed higher level on the top than that close to the adhesion substrate (Fig. 5C). Except two cases, most central cells still revealed the HFLN phenomenon (Fig. 5D–F). The statistical results of the average FSS in the SFC and the SNC showed that most relative values were
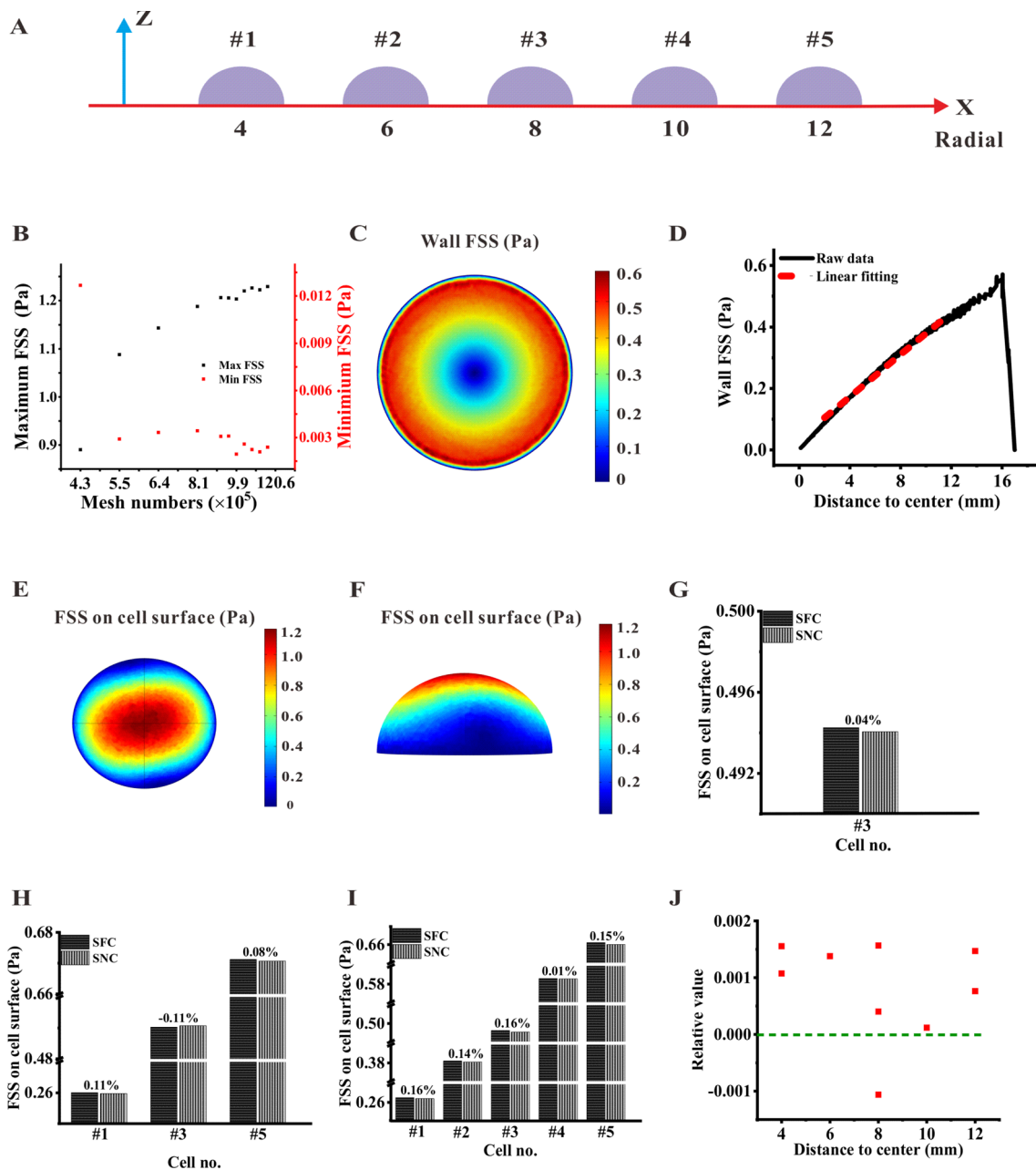
Fig. 3 Average FSS in the SFC and the SNC on discretely distributed cells along the radial direction. **A** Schematic of five cells arranged along the radial direction. **B** Mesh dependency analysis. The one quarter circle in each cell is divided into 26 segments. **C** Wall FSS on the cell surface. **D** Average wall FSS at different distances away from the center and linearly fitted by the dotted red line (goodness of fitting $=0.99207$). **E** Top and **F** side views of FSS on the cell surface. **G–I** Average FSS in the SFC and the SNC in a cell when 1, 3, or 5 cells are placed on the plate along the radial direction. **J** Relative average FSS between the SFC and the SNC. The positive relative value represents that the FSS on the cell surface in the SFC is larger than that in the SNC, whereas the positive relative value is the opposite

positive. If the effect of the secondary flow was not considered, all relative values were positive (Supplementary Fig. 3A–D). The results in the bands with different orientations for central cells showed that the average FSS on the top was smaller than that close to the adhesion substrate (Fig. 6A–J). Statistical results indicated that almost all relative values were positive

and that only one relative value was negative, suggesting that the HFLN phenomenon occurred in most locations around a cell (Fig. 6J and Supplementary Fig. 4A–J). Three kinds of patterning models were constructed to study the effect of different cell spacing values on the relative value of the FSS on the cell surface (Fig. 7A). When the distance between

Fig. 4 Average FSS within the bands with different orientations in the SFC and the SNC on discretely distributed cells. **A–I** Average FSS within the bands with different orientations in the SFC and the SNC in a cell when 1, 3, or 5 cells are placed on the plate along the radial direction. **J** Relative average FSS within the bands between the SFC and the SNC
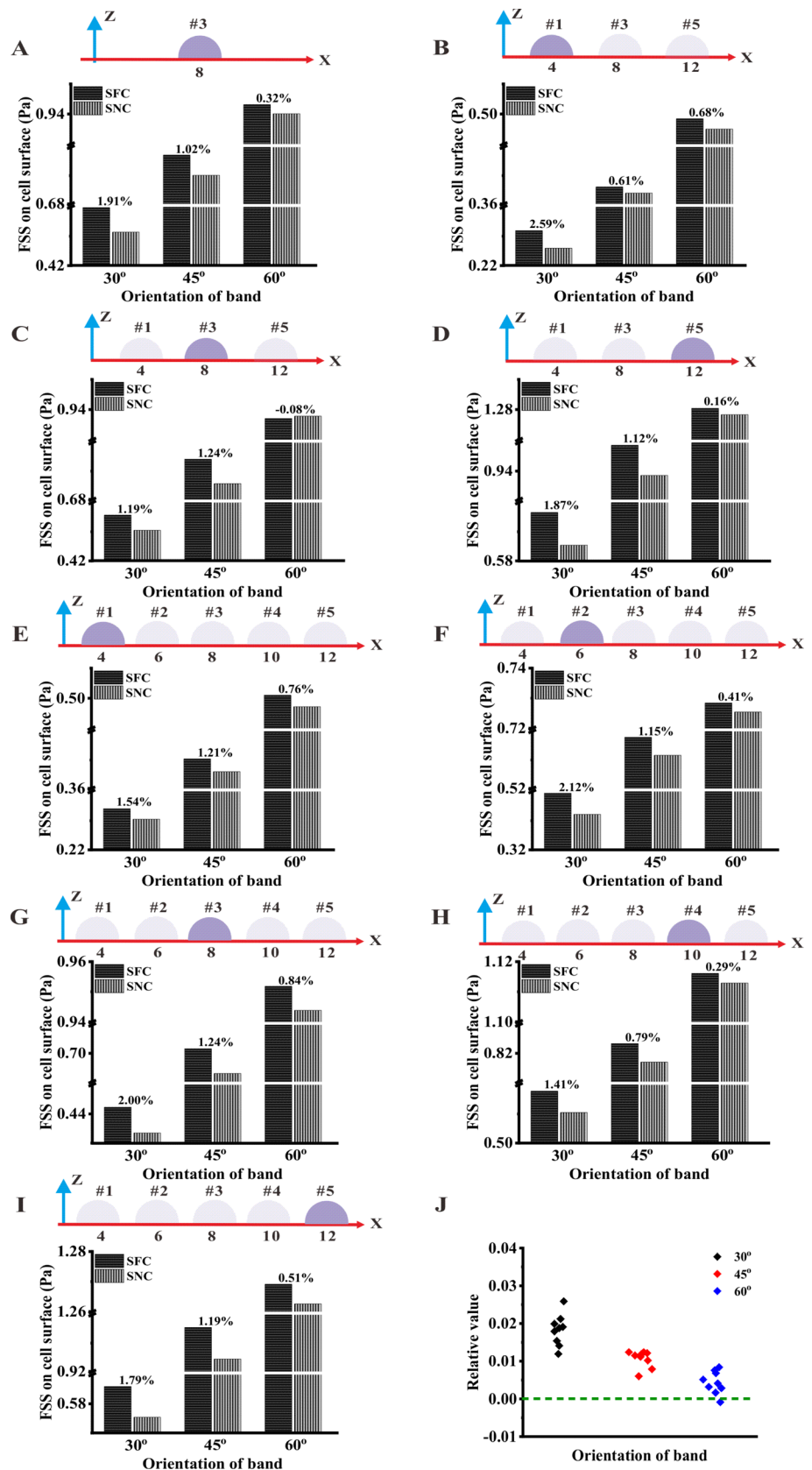
Fig. 5 Average FSS in the SFC and the SNC on hexagonal closely packed cells. **A** Schematic of five cell groups arranged along the radial direction. Central cells are represented by a purple solid circle. **B** Mesh division of one group, in which the mesh of central cell is refined. **C** FSS map on the cell surface for a cell group. **D–F** Average FSS in the SFC and the SNC in 1, 3, and 5 cell groups. **G** Relative average FSS between the SFC and the SNC
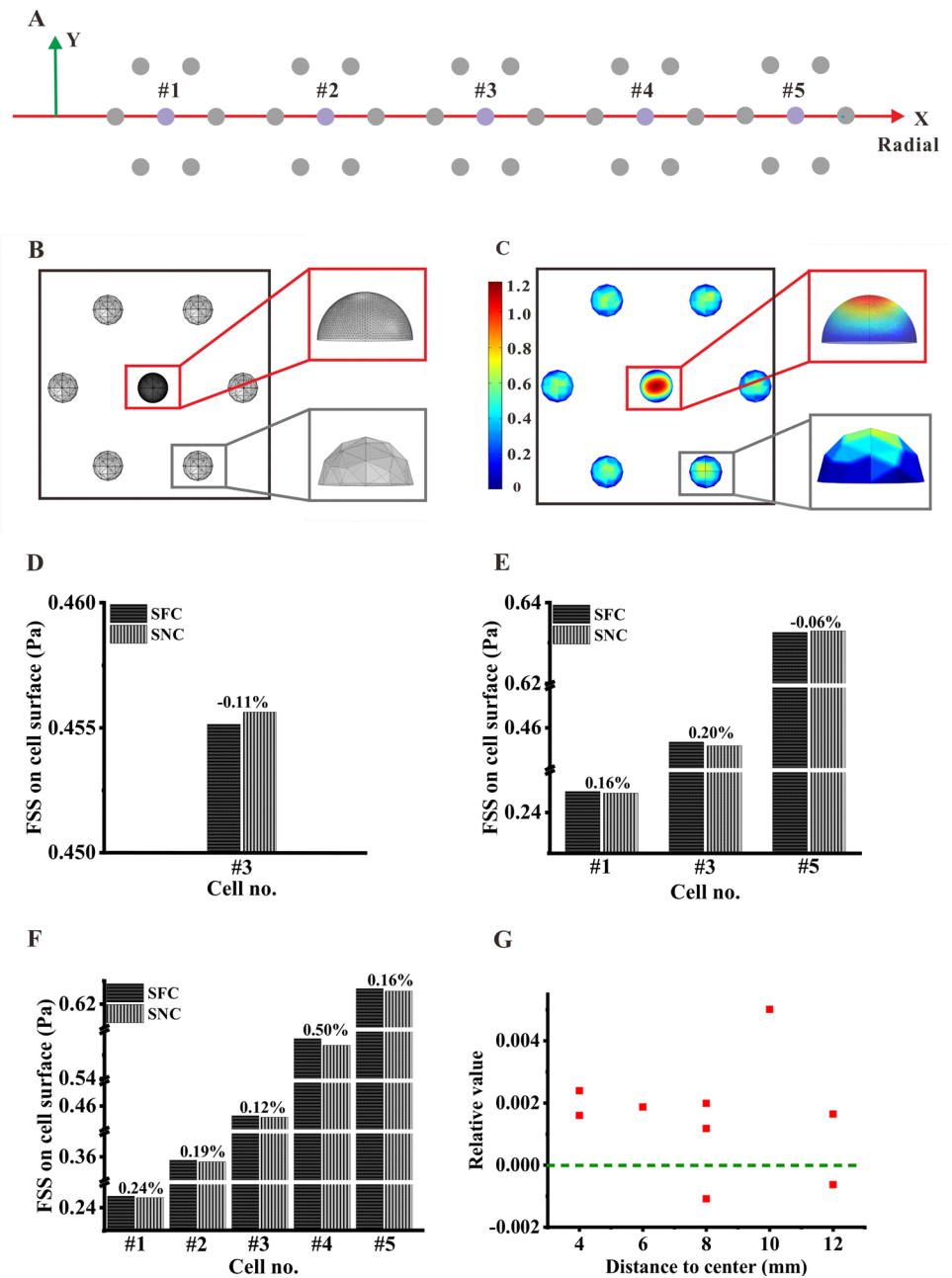

adjacent cells decreased to 0, the relative value of central cells significantly decreased, indicating that the HFLN was reduced (Fig. 7B, C). If the effect of the secondary flow was not considered, the relative values of the FSS in the central cells became negative when the cells in a location were placed together without spacing (Fig. 7D, E).

4 Discussion

This study aims to explain our previous experimental observation that osteoclast precursors move toward the low-FSS area in the gradient FSS field, evidently deviating

Fig. 6 Average FSS within bands with different orientations in the SFC and the SNC on hexagonal closely packed cells. **A–I** Average FSS within the bands with different orientations in the SFC and the SNC in 1, 3, and 5 cell groups. **J** Relative average FSS within the bands between the SFC and the SNC
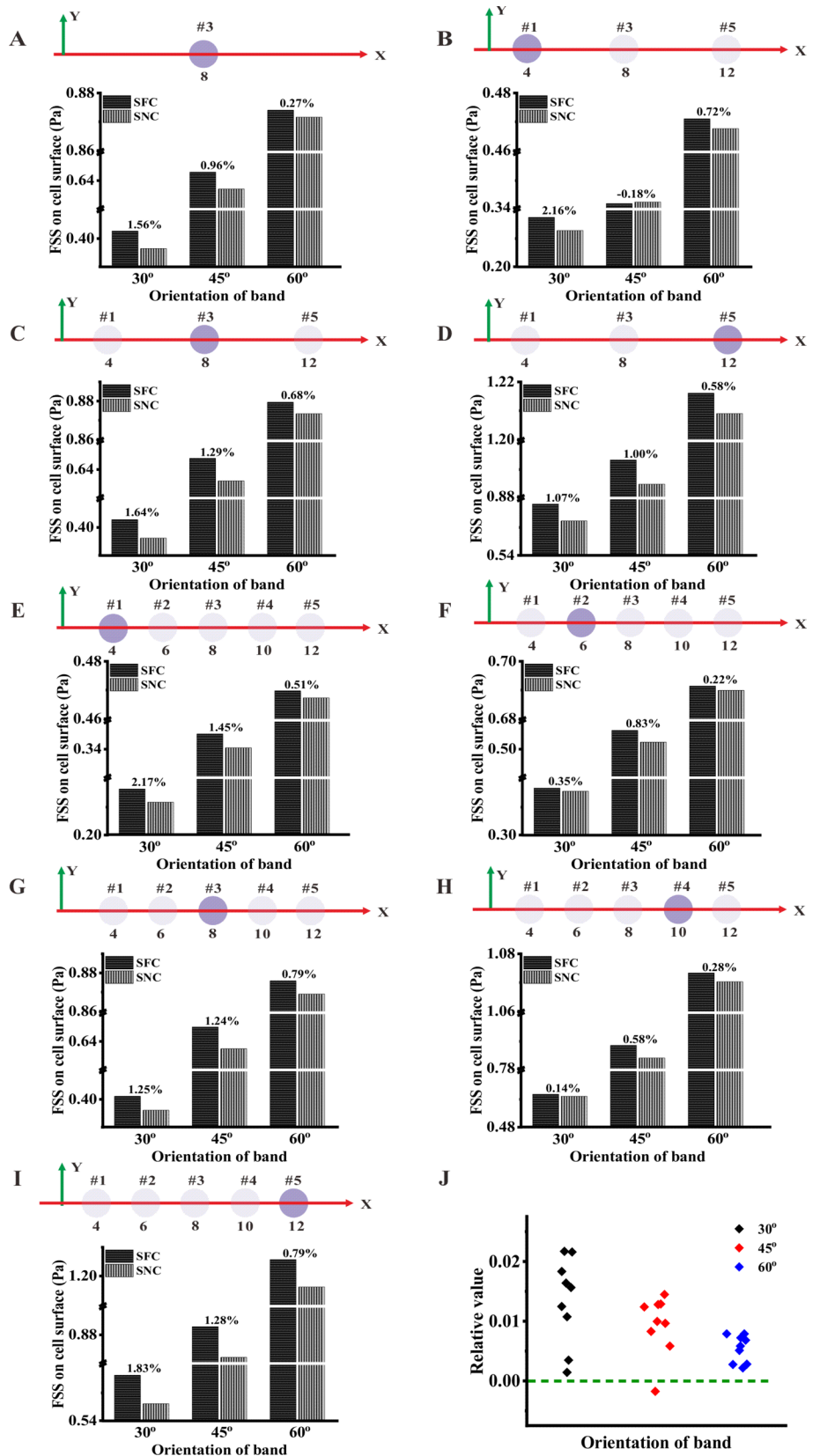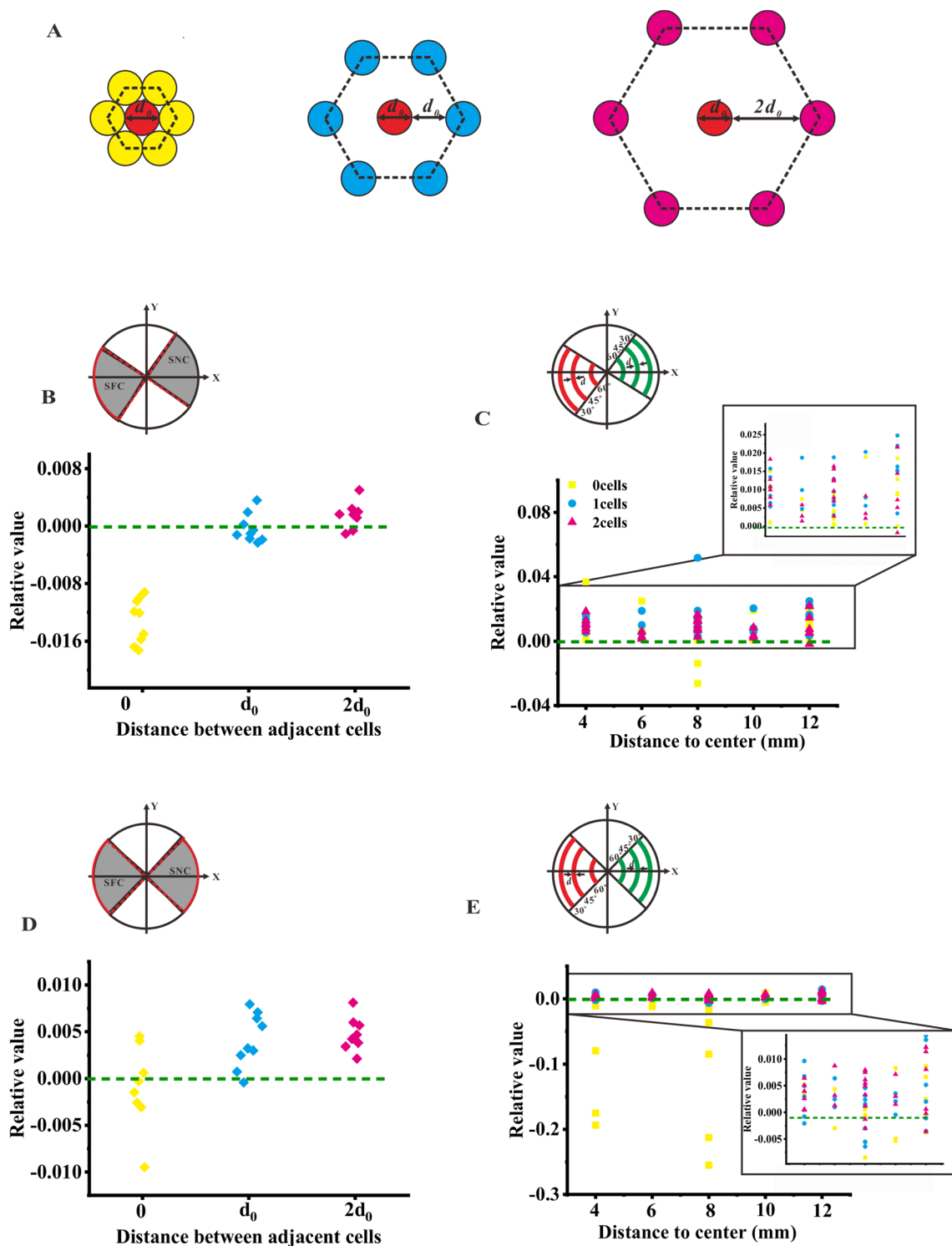
Fig. 7 Effect of cell spacing on the relative FSS in the SFC and the SNC on hexagonal closely packed cells. **A** Schematic of hexagonal closely packed cells with different cell spacing. Relative average FSS (**B**) in the SFC and the SNC on hexagonal closely packed cells with different cell spacing when considering the secondary flow and **C** within bands. Relative average FSS (**D**) in the SFC and the SNC on hexagonal closely packed cells with different cell spacing when the secondary flow is not considered and **E** within bands

from the direction of the actual fluid flow. The custommade cone-and-plate flow chamber is mimicked using the FEA to construct the gradient FSS field, and hyperelastic cells are discretely distributed or hexagonal closely packed on the plate with the gradient FSS. The local FSS on the surface of one cell along the radial direction is computed to reveal whether its intracellular distribution is relevant to the whole FSS distribution on the plate.

The cone–plate configuration has been extensively used in many studies. Cox have obtained the uniform FSS field through the rotation of a cone with linear generatrix (Cox 1962). A novel cone-and-plate flow chamber with truncated generatrix is previously designed, and the FSS field on the plate in this new flow chamber can be controlled compared with that in the traditional system. This cone-and-plate flow chamber is adopted to construct the gradient FSS field and discover that osteoclast precursors move toward the low-FSS region on the plate in this flow chamber (Gao et al. 2019b). The microfluidic technology is also adopted to construct the gradient FSS field, demonstrating that tumor cells prefer to adhere and grow in a curved vessel with the gradient FSS field by activating increased adhesion ligands (Yan et al. 2012).

Several arrangements of cells on the plate are investigated in this study. First, 1, 3, or 5 cells are arranged discretely along the radial direction to mimic the FSS field on the cell surface when no intercellular interaction of flow field is present. Interestingly, most cases have an average FSS in the SFC larger than that in the SNC, indicating that the wholegradient FSS field can cause the gradient FSS distribution in one cell, i.e., so-called HFLN phenomenon. However, some cells with average FSS value in the SFC bands are smaller than those in the SNC bands, which may be due to computation error. In addition, the hexagonal closely packed arrangements with different intercellular spacing values are applied to clarify whether the central cells in one location have the HFLN phenomenon. Results show that when neighboring cells approach central cells, the HFLN distribution of the FSS on central cells is reduced and finally disappears for zero spacing. These results are consistent with our experimental observation that the migration toward the low-FSS region only occurs for the discretely distributed osteoclast precursors.

This gradient FSS-induced HFLN intracellular FSS distribution may be used to explain the migration of osteoclast precursors toward the low-FSS region under the gradient FSS field. Some previous studies have found that the cytosolic calcium concentration is mediated by the fluid flow through mechanosensitive ion channels, such as transient receptor potential channels or Piezo channels (Li et al. 2012, 2014, 2018; Liu et al. 2014; Yoshikawa et al. 1997). In addition, the gradient distribution of intracellular calcium ions regulates the orientation of the cell migration by mediating adhesion molecules (Boudot et al. 2010; Ishii et al. 2010; Koizumi et al. 2009; Wheal et al. 2014). However, whether the calcium ion channels in different locations of the cell membrane are activated by the gradient FSS on the cell surface remains unknown and should be clarified in the future.

Many mechanical models of living cells have been established depending on the cell types or the status to be studied. For example, the cortical shell–liquid core (or liquid drop) models are applied to the suspended cell (Evans and Kukan 1984). The solid model is generally used for adherent cells (Bilodeau 1992; Petersen et al. 1982; Shin and Athanasiou 1999). The power–law structural damping model is suited for studying the dynamic behavior of adherent cells (Alcaraz et al. 2003; Fabry et al. 2001; Mahaffy et al. 2000; Maksym et al. 2000). The biphasic model is widely used to study musculoskeletal cells (Guilak and Mow 2000; Shieh and Athanasiou 2002, 2003). Compared with other models, the most significant feature of the solid model is that the entire cell is usually assumed to be homogeneous, in which the proposed materials include the incompressible elastic solid or the viscoelastic solid. The elastic model is a simplification of the viscoelastic model, in which the time factor is neglected and extensively used in experiments, such as micropipette aspiration, atomic force microscope indentation, cytoindenter, and magnetic bead twisting cytometry (Bilodeau 1992; Mijailovich et al. 2002; Petersen et al. 1982; Shin and Athanasiou 1999; Theret et al. 1988). Several types of cells, including endothelial cells, osteoblasts, and chondrocytes, have been suggested to exhibit the viscoelastic behavior (Guilak and Mow 2000; Jones et al. 1999; Koay et al. 2003; Theret et al. 1988). In the present study, the hyperelastic model with compressible isotropic Hookean material is adopted for the cells, which is simple but accurately describes the mechanical properties of cells in good agreement with AFM experimental data (Sebastian et al. 2020).

In summary, the FEA results in this study show that the gradient FSS field leads to the intracellularly gradient FSS distribution on the cell surface and that the decreased cell spacing reduces this phenomenon. The difference of local FSS on the cell surface under the gradient FSS field may be the fundamental reason for the migration of osteoclast precursors toward the low-FSS region.

Declarations

Conflict of interest We declare that we have no conflicts of interest.

References

Alcaraz J, Buscemi L, Grabulosa M, Trepat X, Fabry B, Farre R, Navajas D (2003) Microrheology of human lung epithelial cells measured by atomic force microscopy. Biophys J 84(3):2071–2079. https://doi.org/10.1016/S0006-3495(03)75014-0

Attard MM (2003) Finite strain—isotropic hyperelasticity. Int J Solids Struct 40(17):4353–4378. https://doi.org/10.1016/S0020-7683(03)00217-8

Bilodeau GG (1992) Regular pyramid punch problem. J Appl Mech 59(3):519–523. https://doi.org/10.1115/1.2893754

Boudot C, Saidak Z, Boulanouar AK, Petit L, Gouilleux F, Massy Z, Brazier M, Mentaverri R, Kamel S (2010) Implication of the calcium sensing receptor and the phosphoinositide 3-kinase/Akt pathway in the extracellular calcium-mediated migration of RAW 264.7 osteoclast precursor cells. Bone 46(5):1416–1423. https://doi.org/10.1016/j.bone.2010.01.383

Cox DB (1962) Radial flow in the cone-plate viscometer. Nature 193:670

Evans E, Kukan B (1984) Passive material behavior of granulocytes based on large deformation and recovery after deformation tests. Blood 64(5):1028–1035. https://doi.org/10.1182/blood.V64.5.1028.1028

Fabry B, Maksym GN, Butler JP, Glogauer M, Navajas D, Fredberg JJ (2001) Scaling the microrheology of living cells. Phys Rev Lett 87(14):148102. https://doi.org/10.1103/PhysRevLett.87.148102

Gao Y, Li TY, Sun Q, Huo B (2019a) Gradient fluid shear stress regulates migration of osteoclast precursors. Cell Adhes Migr 13(1):183–191. https://doi.org/10.1080/19336918.2019.1619433

Gao Y, Li TY, Sun Q, Ye CY, Guo MM, Chen ZB, Chen J, Huo B (2019b) Migration and differentiation of osteoclast precursors under gradient fluid shear stress. Biomech Model Mechanobiol 18(6):1731–1744. https://doi.org/10.1007/s10237-019-01171-z

George D, Allena R, Rémond Y (2018) A multiphysics stimulus for continuum mechanics bone remodeling. Math Mech Complex Syst 6(4):307–319. https://doi.org/10.2140/memocs.2018.6.307

George D, Allena R, Bourzac C, Pallu S, Bensidhoum M, Portier H, Rémond Y (2020) A new comprehensive approach for bone remodeling under medium and high mechanical load based on cellular activity. Math Mech Complex Syst 8(4):287–306. https://doi.org/10.2140/memocs.2020.8.287

Giorgio I, Spagnuolo M, Andreaus U, Scerrato D, Bersani AM (2020) In-depth gaze at the astonishing mechanical behavior of bone: a review for designing bio-inspired hierarchical metamaterials. Math Mech Solids 26(7):1074–1103. https://doi.org/10.1177/1081286520978516

Grover WH, Bryan AK, Diez-Silva M, Suresh S, Higgins JM, Manalis SR (2011) Density-measuring single-cell density. Proc Natl Acad Sci USA 108(27):10992–10996. https://doi.org/10.1073/pnas.1104651108

Guilak F, Mow VC (2000) The mechanical environment of the chondrocyte: a biphasic nite element model of cell matrix interactions in articular cartilage. J Biomech Eng 130(6):061009. https://doi.org/10.1115/1.2978991

Ishii M, Kikuta J, Shimazu Y, Meier-Schellersheim M, Germain RN (2010) Chemorepulsion by blood S1P regulates osteoclast precursor mobilization and bone remodeling in vivo. J Exp Med 207(13):2793–2798. https://doi.org/10.1084/jem.20101474

Jones WR, Ting-Beall PH, Lee GM, Kelley SS, Hochmuth RM, Guilak F (1999) Alterations in the Young's modulus and volumetric properties of chondrocytes isolated from normal and osteoarthritic human cartilage. J Biomech 32(2):119–127. https://doi.org/10.1016/s0021-9290(98)00166-3

Koay EJ, Shieh AC, Athanasiou KA (2003) Creep indentation of single cells. J Biomech Eng 125(3):334–341. https://doi.org/10.1115/1.1572517

Koizumi K, Saitoh Y, Minami T, Takeno N, Tsuneyama K, Miyahara T, Nakayama T, Sakurai H, Takano Y, Nishimura M, Imai T, Yoshie O, Saiki I (2009) Role of CX3CL1/fractalkine in osteoclast differentiation and bone resorption. J Immunol 183(12):7825–7831. https://doi.org/10.4049/jimmunol.0803627

Li P, Hu M, Sun S, Zhang Y, Gao Y, Long M, Huo B, Zhang D (2012) Fluid flow-induced calcium response in early or late differentiated osteoclasts. Ann Biomed Eng 40(9):1874–1883. https://doi.org/10.1007/s10439-012-0554-z

Li P, Liu C, Hu M, Long M, Zhang D, Huo B (2014) Fluid flow-induced calcium response in osteoclasts: signaling pathways. Ann Biomed Eng 42(6):1250–1260. https://doi.org/10.1007/s10439-014-0984-x

Li P, Bian X, Liu C, Wang S, Guo M, Tao Y, Huo B (2018) STIM1 and TRPV4 regulate fluid flow-induced calcium oscillation at early and late stages of osteoclast differentiation. Cell Calcium 71:45–52. https://doi.org/10.1016/j.ceca.2017.12.001

Liu CL, Li SN, Ji BH, Huo B (2014) Flow-induced migration of osteoclasts and regulations of calcium signaling pathways. Cell Mol Bioeng 8(1):213–223. https://doi.org/10.1007/s12195-014-0372-5

Mahaffy RE, Shih CK, MacKintosh FC, Kas J (2000) Scanning probe-based frequency-dependent microrheology of polymer gels and biological cells. Phys Rev Lett 85(4):880–883. https://doi.org/10.1103/PhysRevLett.85.880

Maksym GN, Fabry B, Butler JP, Navajas D, Tschumperlin DJ, Laporte JD, Fredberg JJ (2000) Mechanical properties of cultured human airway smooth muscle cells from 0.05 to 0.4 Hz. J Appl Physiol 89(4):1619–1632. https://doi.org/10.1152/jappl.2000.89.4.1619

McAllister TN, Du T, Frangos JA (2000) Fluid shear stress stimulates prostaglandin and nitric oxide release in bone marrow-derived preosteoclast-like cells. Biochem Biophys Res CO 270(2):643–648. https://doi.org/10.1006/bbrc.2000.2467

McGarry, JG, Prendergast, PJ (2004) A three-dimensional finite element model of an adherent eukaryotic cell. Eur Cells Mater 16(7):27–34. https://doi.org/10.22203/eCM.v007a03

Mijailovich SM, Kojic M, Zivkovic M, Fabry B, Fredberg JJ (2002) A finite element model of cell deformation during magnetic bead twisting. J Appl Physiol 93(4):1429–1436. https://doi.org/10.1152/japplphysiol.00255.2002

Petersen NO, McConnaughey WB, Elson EL (1982) Dependence of locally measured cellular deformability on position on the cell. Proc Natl Acad Sci USA 79(17):5327–5331. https://doi.org/10.1073/pnas.79.17.5327

Robling AG, Castillo AB, Turner CH (2006) Biomechanical and molecular regulation of bone remodeling. Annu Rev Biomed Eng 8:455–498. https://doi.org/10.1146/annurev.bioeng.8.061505.095721

Sdougos HP, Bussolari SR, Dewey CF (2006) Secondary flow and turbulence in a cone-and-plate device. J Fluid Mech 138:379–404. https://doi.org/10.1017/s0022112084000161

Sebastian JM, Franziska W, Carina B, Christian B, Albrecht K, Gekle S (2020) A hyperelastic model for simulating cells in flow. Biomech Model Mechanobiol 20(2):509–520. https://doi.org/10.1007/s10237-020-01397-2

Shieh AC, Athanasiou KA (2002) Biomechanics of single chondrocytes and osteoarthritis. Crit Rev Biomed Eng 30(4–6):307–343. https://doi.org/10.1615/critrevbiomeng.v30.i456.40

Shieh AC, Athanasiou KA (2003) Principles of cell mechanics for cartilage tissue engineering. Ann Biomed Eng 31(1):1–11. https://doi.org/10.1114/1.1535415

Shin D, Athanasiou K (1999) Cytoindentation for obtaining cell biomechanical properties. J Orthop Res 17(6):880–890. https://doi.org/10.1002/jor.1100170613

Simo JC, Pister KS (1984) Remarks on rate constitutive equations for finite deformation problems: computational implications. Comput Methods Appl Mech Eng 46:201–205. https://doi.org/10.1016/0045-7825(84)90062-8

Theret DP, Levesque MJ, Sato M, Nerem RM, Wheeler LT (1988) The application of a homogeneous half-space model in the analysis of endothelial cell micropipette measurements. J Biomech Eng 110(3):190–199. https://doi.org/10.1115/1.3108430

Wheal BD, Beach RJ, Tanabe N, Dixon SJ, Sims SM (2014) Subcellular elevation of cytosolic free calcium is required for osteoclast migration. J Bone Miner Res 29(3):725–734. https://doi.org/10.1002/jbmr.2068

Xue F, Lennon AB, McKayed KK, Campbell VA, Prendergast PJ (2015) Effect of membrane stiffness and cytoskeletal element density on mechanical stimuli within cells: an analysis of the consequences of ageing in cells. Comput Methods Biomech Biomed Eng 18(5):468–476. https://doi.org/10.1080/10255842.2013.811234

Yan WW, Cai B, Liu Y, Fu BM (2012) Effects of wall shear stress and its gradient on tumor cell adhesion in curved microvessels. Biomech Model Mechan 11(5):641–653. https://doi.org/10.1007/s10237-011-0339-6

Ye CY, Ali S, Sun Q, Guo MM, Liu Y, Gao Y, Huo B (2019) Novel cone-and-plate flow chamber with controlled distribution of wall fluid shear stress. Comput Biol Med 106:140–148. https://doi.org/10.1016/j.compbiomed.2019.01.014

Yoshikawa N, Ariyoshi H, Ikeda M, Sakon M, Kawasaki T, Monden M (1997) Shear-stress causes polarized change in cytoplasmic calcium concentration in human umbilical vein endothelial cells. Cell Calcium 22(3):189–197. https://doi.org/10.1016/S0143-4160(97)90012-9